Soft-Body Robot Fish

Pablo Valdivia y Alvarado and Kamal Youcef-Toumi

Abstract New mechanism paradigms are needed to improve robot performance and resilience in harsh environments. Soft continuous mechanisms can be simpler and more robust than the stiff-discrete assemblies traditionally found in robotics. Herein, a methodology to design underactuated soft robots is presented and its application to fish-like robots is outlined. The principle is simple, a flexible viscoelastic continuous body is designed with the appropriate material heterogeneity such that dominant modes of vibration match desired body motions. Design examples are given for different fish-like robots and actuation units. Fabrication techniques and testing procedures are presented along with locomotion performance. The approach is general and can be applied to bodies with more complex target kinematics and offers a promising alternative for mobile robots.

1 The Need for New Robot Bodies

Many field applications would benefit from unmanned systems that can function and survive for extended periods of time in harsh and unstructured liquid environments. Oceans are a prime example, marine environments are extremely unforgiving on hardware. All marine-bound equipment requires periodic maintenance which limits deployment cycle times. Environment complexity and deployment scale add further challenges. As a result, autonomous marine robots require excellent locomotion efficiency, mechanical robustness, and maneuverability to survive and successfully accomplish mission goals.

P. Valdivia y Alvarado (✉) · K. Youcef-Toumi
Mechanical Engineering Department, Massachusetts Institute of Technology, Cambridge, MA, USA
e-mail: pablov@mit.edu

K. Youcef-Toumi
e-mail: youcef@mit.edu

R. Du et al. (eds.), *Robot Fish*, Springer Tracts in Mechanical Engineering,
DOI 10.1007/978-3-662-46870-8_6

Biology is inspiring a wide range of promising locomotion approaches that could potentially address these requirements. However, new hardware paradigms are needed to take full advantage of these approaches. Bio-inspired locomotion requires mechanisms with large numbers of degrees of freedom (DOF) to efficiently transfer momentum to a liquid environment. This poses significant problems as the added mechanical complexity can prevent long-term deployments. If mechanical transmissions are not properly sealed and protected from the environment, corrosion and biofouling can quickly degrade components and prevent long-term deployments. Simplicity and mechanical robustness are key for prolonging hardware survival.

1.1 Rigid and Discrete Versus Soft and Continuous

Traditional robot bodies are rigid and discrete, mechanisms consist of assemblies of gears, pulleys, cables, linkages, etc. As a result, the complexity of mechanical transmissions increases with required DOFs. This can be detrimental to the mechanical robustness of a robot as the probabilities of failure increase with mechanism part count.

In contrast, the natural dynamics of a soft flexible body can be exploited to reduce mechanism complexity. The modes of vibration of a structure depend on geometry, material properties, and excitation (i.e., forces being applied). Hence, a structure can be designed such that the dominant modes of vibration match desired body motions when a reduced number of actuation inputs is applied. If successful, such a mechanism is in principle simple and robust as it only consists of a flexible body and an excitation source. To illustrate this idea, Fig. 1 shows the differences between the traditional approach of designing a fish robot and the proposed

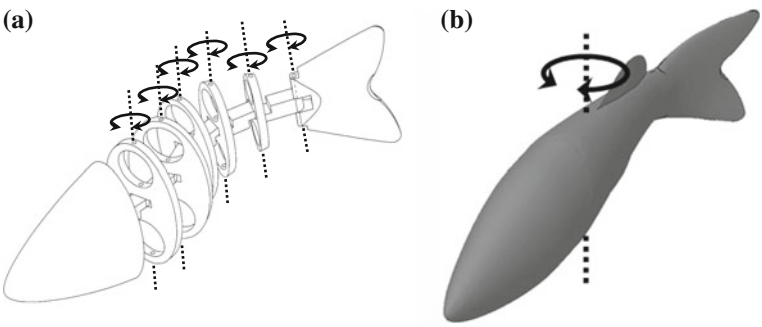

Fig. 1 Traditional discrete-stiff mechanism versus underactuated soft body continuous mechanism approach for a robotic fish: **a** The body undulations needed for locomotion are traditionally replicated using manipulator-like mechanisms with actuators driving each DOF directly or through pulleys, linkages, or geared transmissions; **b** in contrast, a soft body can be manufactured with the appropriate material heterogeneity such that its dominant modes of vibration match the required body motions when excited by a reduced number of actuators

underactuated soft body approach. The body undulations required for fish-like locomotion are traditionally replicated using manipulator-like mechanisms with actuators driving each DOF directly or through transmissions involving pulleys, cables, linkages, and gears. Alternatively, a soft body can be manufactured with a material heterogeneity such that its natural dynamic response matches desired body motions. In addition, a continuous soft body provides better protection from the environment for delicate components as all mechanisms are encapsulated and protected inside the body.

1.2 Previous Work

The basic principles of the underactuated soft body approach, applied to fish-like robots, were first proposed by Valdivia y Alvarado and Youcef-Toumi in [28, 29], and subsequently formalized in [21, 30]. The approach relies on two principles: using soft bodies instead of traditional stiff mechanisms, and allowing passive mechanism dynamics achieve target motions. Earlier work in the areas of manufacturing, passive robotic mechanisms, and biomimetics enabled crucial tools and principles for developing the approach.

Fabricating heterogeneous mechanisms traditionally involves assembling different discrete components and addressing issues related to fastening, sealing, and wear due to friction. Additive prototyping ideas such as shape deposition manufacturing [18] enabled simultaneous fabrication and assembly of components and mechanisms with complex geometries and heterogeneous materials. The tools and techniques developed allowed the manufacture of complex continuum structures and marked a shift away from the lumped-parameter type mechanisms prevalent in automation.

The control of dynamic systems benefits from the knowledge of the physics governing the problem. The idea of exploiting mechanism and environment dynamics to achieve control goals was famously explored by Mcgeer on passive dynamic walkers [17]. Kubow and Full [14] studied similar concepts on cockroach legs. Having the dynamic system play a role in control is a very powerful tool that enables simplification of both mechanism and overall control requirements.

Finally, animal locomotion has provided inspiration for mobile robot design and control in many different areas. Applications in liquid environments sparked interest on fish-like locomotion given its perceived high efficiency. The work by Barrett et al. [4] inspired the development of fish-like robots to understand the hydrodynamics involved in fish locomotion and to develop new mobile robot platforms. Work on fish-like robots has benefited from many different approaches, and as a result they represent an ideal platform to test underactuated soft robot ideas.

Herein, the main points of the underactuated soft body approach are presented along with representative performance measurements. Several practical considerations are discussed and suggestions for further work are presented. With advances in the fields of material synthesis and actuation new and exciting applications of these ideas are emerging.

2 Design Methodology

The main goal of the design methodology is to identify the proper material heterogeneity needed in a soft body to achieve modes of vibration that match desired body motions. The methodology consists of five steps:

(i) Model desired body or appendage kinematics. Derive models of the motions required to achieve the desired locomotion performance. As seen in Fig. 2, these motions can involve only a section of the body, in the case of an appendage, or the entire body.
(ii) Model soft body dynamics. Derive continuum mechanics models of the dynamics (vibrations) in a flexible viscoelastic body. The models usually involve a system of partial differential equations and their complexity is determined by the assumptions regarding geometry and deformation.
(iii) Plug in desired kinematics into dynamic models. The approach does not attempt to find the system response by solving the dynamic equations. The desired solutions, the motions of interest, are the kinematic equations found in (i). Kinematic models can be plugged into the dynamic equations and boundary conditions transforming a set of partial differential equations into a set of algebraic and trigonometric equations.
(iv) Use appropriate constraints to solve the system of equations. For locomotion in fluid environments maintaining neutral buoyancy is important and characteristic geometrical features must also be conserved to achieve the hydrodynamics of interest. These constraints narrow the choices on the density of the materials used and body geometry.

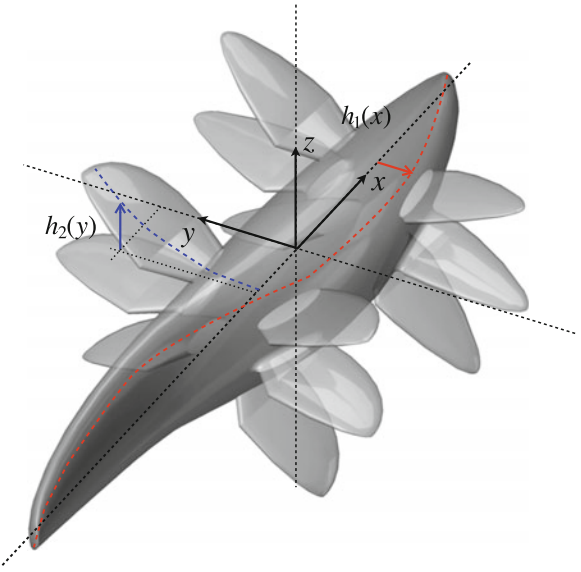

Fig. 2 Design methodology: the body or appendage dynamics of a biological creature is of interest to improve the locomotion performance of man-made vehicles, the kinematics of interest and the dynamics of a flexible body are modeled, the desired motions (e.g., $h_1(x)$, $h_2(y)$) are inserted into a dynamic model to solve for the required material distributions

(v) Solve for model parameters. Finally, an actuation distribution (number, location, magnitude, and frequency) is prescribed and the system of equations is solved using the desired constraints. The model parameters solved for are the material properties of the continuum: modulus and viscosity distributions.

The design methodology is set up as an inverse problem. Rather than solving for the response of a dynamic system (e.g., soft flexible body), model parameters that can enable desired system responses are identified.

To illustrate the approach, in the remainder of this section the design methodology is applied to the design of carangiform (e.g., bass) and thunniform (e.g., tunas) robotic fish. According to the classification of fish swimming modes by Breder [5], carangiform and thunniform fish use mostly tail and caudal fin motions for propulsion. Earlier studies focused on these swimming modes due to their presumed high hydrodynamic efficiencies [4].

2.1 Modeling Body Kinematics

Figure 3 shows the outline of a fish-like viscoelastic body of length l moving at an average speed U. Body motions are described with respect to a Cartesian (x, y, z) reference frame attached to the body frontal end. Carangiform and thunniform fish swim by propagating traveling waves along the length of their bodies. The body traveling wave moves down the body at a speed V and has a wavelength λ. Barrett

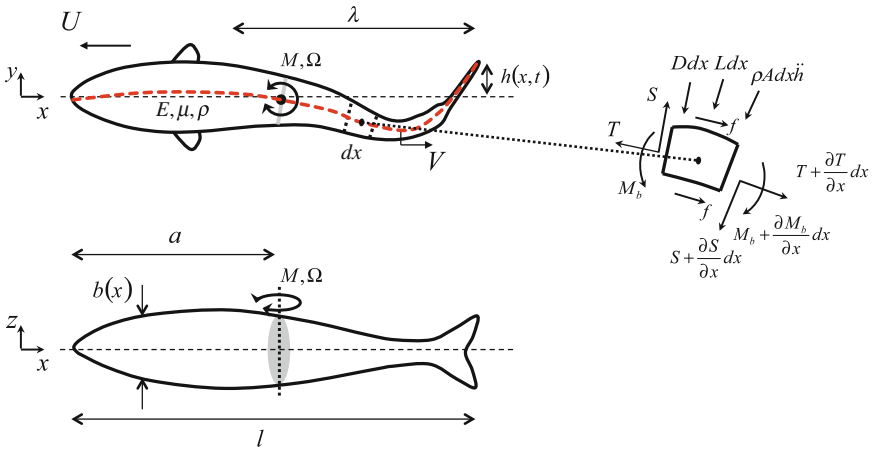

Fig. 3 Fish model: *Top* and *side views* of a fish-like body of length l moving forward at an average speed U. Lateral body motions $h(x,t)$ in the body frame of reference take the form of traveling waves with a constant wavelength λ. A concentrated moment of magnitude M and actuation frequency Ω located at a distance $x = a$ excites body motions. The free body diagram of a section of the body shows relevant forces

et al. [4] proposed a simple model for the body center line lateral deflections h of the form: $h(x,t) = H(x)\sin(\omega t - \kappa x)$, where $H(x) = c_1 x + c_2 x^2$ is an amplitude envelope, ω is the caudal fin flapping frequency, and $\kappa = 2\pi/\lambda$ is the wave number. Valdivia y Alvarado [21] proposed a slightly different model using $H(x) = a_1 + a_2 x + a_3 x^2$ instead, which could be used to describe both carangiform and thunnifrom swimming modes (values for a_1, a_2, and a_3 depend on fish swimming mode). These models are reasonable approximations of fish kinematics in the body frame of reference. For analysis in an inertial reference frame rigid body motions (rotations $h_r(t)x$ and translations $h_t(t)$) must be added [15]. The kinematics can then be modeled as,

$$h(x,t) = H(x)\sin(\omega t - \kappa x) + h_t(t) + h_r(t)x, \tag{1}$$

h_t and h_r can be found using the problem boundary conditions. To facilitate calculations, in this study the definition of the amplitude envelope used is modified to $H(x) = c_1\cos(c_2 x) + c_3$ (values for c_1, c_2, and c_3 also depend on fish swimming mode). All relevant model parameters are listed in Table 1 along with their definitions. Values for the parameters in Eq. (1) for both fish swimming modes are listed in Table 2 (c_i values are given only for carangiform swimming mode). Figure 4 shows the center line body planar kinematics described by Eq. (1) at four different times, $t = \{\tau/4, \tau/2, 3\tau/4, \tau\}$, during the tail flapping period τ. The amplitude envelope $H(x)$ is shown as dashed black lines. Outlines of the body during the same times are shown in the upper portion of the figure.

2.2 Modeling Body Dynamics

Figure 3 also shows the forces acting on a section of the fish-like viscoelastic body as it is actuated to move by a concentrated moment M_a. The body is assumed to have an elliptical cross section with major and minor radii $R(x)$ and $r(x)$, respectively. For simplicity, bending is assumed to be the dominant deformation mode. Hence, when the concentrated moment is located at a distance $x = a$ from the body front end, $M_a = \delta'(x-a)\,M\sin(\Omega t)$, the dynamics governing body lateral vibrations, $h(x,t)$, are given by [21],

$$\frac{\partial^2}{\partial x^2}\left(EI\frac{\partial^2 h}{\partial x^2} + \mu I\frac{\partial^2 h}{\partial t \partial x^2}\right) = -L - \rho A\frac{\partial^2 h}{\partial t^2} + \delta'(x-a)M\sin(\Omega t)\,, \tag{2}$$

where E, μ, and ρ are the modulus of elasticity, the viscosity, and the density of the materials along the flexible body. $A = \pi R(x)r(x)$ and $I = \frac{\pi}{4}R(x)r(x)^3$ are the local cross-sectional area and the second moment of area of the fish-like body. In this analysis, E and μ are assumed to be functions of x only, and ρ is assumed to be constant throughout the body length. The hydrodynamic force L acting on the body surface is approximated by the added mass effects [21],

Table 1 Model parameters

Parameter	Definition	Units
A	Cross-sectional area at x	(m^2)
a	Location of concentrated actuation moment	(m)
a_1, a_2, a_3	Variables defining the amplitude envelope	$(\mathrm{m}), (-), (\mathrm{m}^{-1})$
b	Body depth at x	(m)
β	Added mass coefficient	$(-)$
C_d	Body drag coefficient	$(-)$
c_1, c_2, c_3	Alternative variables to define amplitude envelope	$(\mathrm{m}), (\mathrm{rad/m}), (\mathrm{m})$
E	Body modulus of elasticity (a function of x only)	$\left(\mathrm{N/m}^2\right)$
ε	Body strain	$(-)$
η	Forward propulsive efficiency	$(-)$
H	Amplitude enveloped	(m)
H_l	Caudal fin peak-to-peak flapping amplitude	(m)
h	Body lateral deflections (a function of x and t)	(m)
I	Second moment of area at x	(m^4)
i	Current consumed by all actuators	(A)
κ	Wave number, $\kappa = 2\pi/\lambda$	(rad/m)
L	Hydrodynamic force normal to the body surface	(N)
l	Body length	(m)
λ	Wavelength of body traveling wave	(m)
M_a	Concentrated actuation moment	(Nm)
M	Magnitude of concentrated actuation moment	(Nm)
m	Added mass (a function of x only)	(kg)
μ	Body viscosity (a function of x only)	(Pa s)
Ω	Frequency of actuation moment	(rad/s)
ω	Caudal fin flapping frequency	(rad/s)
R	Body cross section major radius (a function of x only)	(m)
r	Body cross section minor radius (a function of x only)	(m)
ρ	Body density (assumed to be constant)	$\left(\mathrm{kg/m}^3\right)$
ρ_f	Density of liquid medium	$\left(\mathrm{kg/m}^3\right)$
T	Forward propulsive force (thrust)	(N)
t	Time	(s)
τ	Caudal fin flapping period	(s)
U	Average forward swimming speed	(m/s)
V	Backward propagating speed of traveling wave	(m/s)
v	Voltage input to all actuators	(V)

Table 2 Parameters for the two proposed kinematic models

Swimming mode	κ	a_1	a_2	a_3	c_1	c_2	c_3
Carangiform	$\frac{7}{l}$	$\frac{0.004\omega l}{2\pi}$	$-\frac{0.02\omega}{2\pi}$	$\frac{0.04\omega}{2\pi l}$	$\frac{\cos^{-1}(0.13l-1)-\pi}{7l/10}$	$\pi - c_1 0.3l$	$1 + 0.2l$
Thunniform	$\frac{9}{l}$	$0.02l$	-0.12	$\frac{0.2}{l}$			

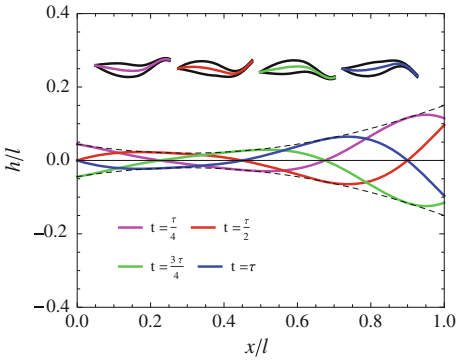

Fig. 4 Fish-like body kinematics as described in Eq. (1). Body center line is shown at four different times during the swimming cycle. *Dashed black lines* show the amplitude envelope $H(x)$. Outlines of a fish-like body during the same cycle times are also shown

$$L \approx m\frac{\partial^2 h}{\partial t^2} \tag{3}$$

where $m = \frac{1}{4}\beta\pi b^2\rho_f$ is the added mass of a cross section at x, β is a geometry dependent constant, $b = 2R(x)$ is the body depth at x, and ρ_f is the density of the fluid medium. Equation (2) assumes that the constitutive relations for the visco-elastic body materials are of the form,

$$\sigma = E\varepsilon + \mu\frac{\partial \varepsilon}{\partial t}. \tag{4}$$

where σ and ε are stress and corresponding strain of the materials. Since the fish-like body is moving freely in a liquid medium both shear and moments at the body ends ($x = 0$ and $x = l$) must be zero. The corresponding boundary conditions can be defined as [21],

$$\begin{aligned}
\left[EI\frac{\partial^2 h}{\partial x^2} + \mu I\frac{\partial^2 h}{\partial t \partial x^2} - M_a\right]_{x=0} &= 0 \\
\left[EI\frac{\partial^2 h}{\partial x^2} + \mu I\frac{\partial^2 h}{\partial t \partial x^2} - M_a\right]_{x=l} &= 0 \\
\left[\frac{\partial}{\partial x}\left(EI\frac{\partial^2 h}{\partial x^2} + \mu I\frac{\partial^2 h}{\partial t \partial x^2} - M_a\right)\right]_{x=0} &= 0 \\
\left[\frac{\partial}{\partial x}\left(EI\frac{\partial^2 h}{\partial x^2} + \mu I\frac{\partial^2 h}{\partial t \partial x^2} - M_a\right)\right]_{x=l} &= 0
\end{aligned} \tag{5}$$

Internal components (batteries, actuators, sensors, etc.) have different densities. To account for the effects of embedded hardware a simple modification in the main dynamic equations is needed. In the case of a fish-like body, Eq. (2) can be modified to,

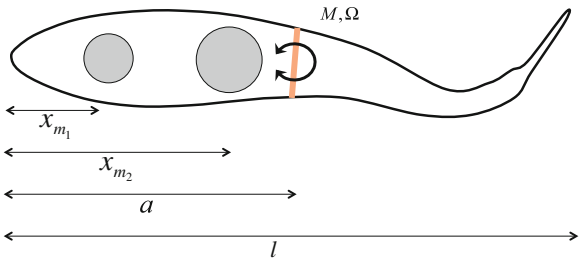

Fig. 5 Batteries and other components can be modeled as lumped masses inside a flexible body. The example in the figure shows two regions of concentrated mass as *two gray circles*. Their contributions to the dynamic behavior is described by Eq. (6)

$$\frac{\partial^2}{\partial x^2}\left(EI\frac{\partial^2 h}{\partial x^2}+\mu I\frac{\partial^2 h}{\partial t\partial x^2}\right)=-L-\left(\rho A+\sum_{i=0}^{n}\delta(x-x_{m_i})m_i\right)\frac{\partial^2 h}{\partial t^2}+\delta'(x-a)M\sin(\Omega t) \tag{6}$$

where the summation term accounts for the lumped masses, m_i, of n embedded component, located at distances x_{m_i} along the body. Figure 5 shows a modified body model example with two concentrated masses; m_1 and m_2.

The dynamic models in Eqs. (2) and (6) account for bending deformations only. However, shear and inertia terms can have large contributions and should be included when implementing body motions involving large curvature variations. Timoshenko and Cosserat beam models are examples of more detailed dynamic descriptions that account for these terms and can enhance the analysis accuracy [2, 20]. Cosserat theory can also be used for more complex three-dimensional kinematics.

2.3 Problem Constraints

Material and geometrical constraints must also be imposed. To facilitate depth control, the body should have a constant density ρ close to the density of the liquid medium ρ_f,

$$\rho \approx \rho_f. \tag{7}$$

It is also important for the body geometry to maintain particular features that enable characteristic fish hydrodynamics. In particular, carangiform body features include a streamlined front end, a large concentration of volume and mass toward the front of the body immediately behind the nose, a tapering peduncle region, and a high aspect ratio caudal fin. Thunniform bodies present a more streamlined body

Table 3 Body geometry parameters

Swimming mode	R_1	R_2	R_3	R_4	r_1	r_2	r_3	r_4
Carangiform	$0.14l$	$\frac{2\pi}{1.6l}$	$0.00008l$	$\frac{2\pi}{1.1l}$	$0.045l$	$\frac{2\pi}{1.25l}$	$0.06l$	$\frac{2}{l}$
Thunniform	$0.1l$	$\frac{2\pi}{1.57l}$	$0.00008l$	$\frac{2\pi}{0.81l}$	$0.055l$	$\frac{2\pi}{1.25l}$	$0.08l$	$\frac{2}{l}$

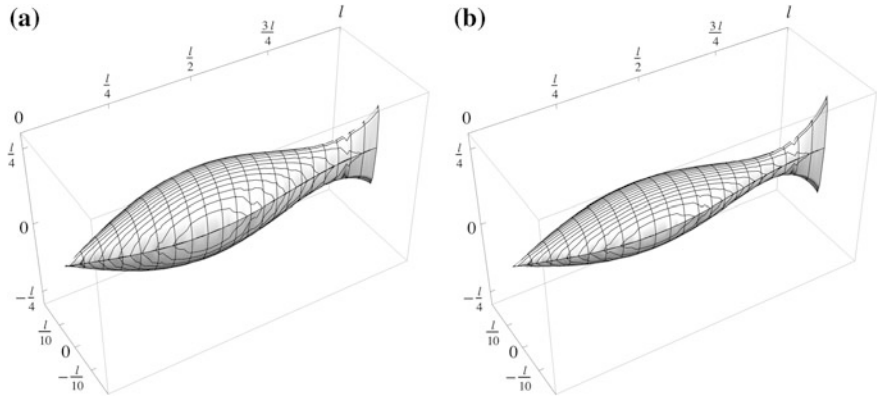

Fig. 6 **a** Fish body geometry for a carangiform model based on Eq. (8). **b** Fish body geometry for a thunniform model based on Eq. (8). Thunniform geometry has a more streamlined profile with a thinner peduncle and a higher aspect ratio caudal fin

with a thinner peduncle and a higher aspect ratio caudal fin with a lunate shape. For carangiform and thunniform swimmers, geometrical features can be modeled using the following expressions for the major and minor body cross-sectional radii [21],

$$\begin{aligned} R(x) &= R_1 \sin(R_2 x) + R_3(e^{R_4 x} - 1) \\ r(x) &= r_1 \sin(r_2 x) + r_3 \sin(r_4 x) \end{aligned} \tag{8}$$

Values for the parameters R_i and r_i, for both carangiform and tunniform bodies, are listed in Table 3. Example geometries for both body types, as defined by Eq. (8), are shown in Fig. 6. Pectoral, dorsal, and anal fins are omitted for now as the analysis concerns forward motion which is achieved primarily through body and caudal fin motions.

2.4 Solving the Inverse Problem

The design objective is to find the material distributions along a viscoelastic body such that its forced vibrations match required body motions. In the case presented here, the desired forward swimming fish kinematics, described in Eq. (1), are

plugged in Eqs. (2), (3), and (5), which describe the dynamics governing the motions of the body. Equation (2) is used rather than Eq. (6) for simplicity but the approach to solving the problem is the same.

Assuming the system is linear, the frequency of body oscillations should match the actuation frequency, thus $\Omega = \omega$. After integrating Eq. (2) twice, it can be rewritten as,

$$\begin{aligned}&\cos(\omega t)[EI\gamma_3 + \mu I\omega\gamma_4] + \sin(\omega t)[EI\gamma_4 - \mu I\omega\gamma_3 - u(x-a)M] \\ &\quad = \cos(\omega t)S_1 + \sin(\omega t)S_2\end{aligned} \tag{9}$$

where $u(x-a)$ is a unit step function and γ_3, γ_4, S_1, and S_2 are given by,

$$\begin{aligned}\gamma_3 &= \left(\frac{\partial^2 H}{\partial x^2} - H\kappa^2\right)\cos(\kappa x) - 2\frac{\partial H}{\partial x}\kappa\sin(\kappa x) \\ \gamma_4 &= \left(\frac{\partial^2 H}{\partial x^2} - H\kappa^2\right)\sin(\kappa x) - 2\frac{\partial H}{\partial x}\kappa\cos(\kappa x) \\ S_1 &= \int_0^l\int_0^l [(\rho A + m)H\omega^2\cos(\kappa x)]\mathrm{d}x\mathrm{d}x \\ S_2 &= \int_0^l\int_0^l [(\rho A + m)H\omega^2\sin(\kappa x)]\mathrm{d}x\mathrm{d}x\end{aligned} \tag{10}$$

Expressions for $E(x)$ and $\mu(x)$ are found for a particular design frequency, ω_d, by solving the trigonometric relation in Eq. (9),

$$\begin{aligned}E(x) &= \frac{S_1\gamma_3 + S_2\gamma_4 + u(x-a)M\gamma_4}{I(\gamma_3^2 + \gamma_4^2)} \\ \mu(x) &= \frac{S_1\gamma_4 - S_2\gamma_3 - u(x-a)M\gamma_3}{I\omega(\gamma_3^2 + \gamma_4^2)}\end{aligned} \tag{11}$$

Solution examples for a carangiform body shape of length $l = 1$ m and forward swimming kinematics as defined in Table 3 (with $\omega = \omega_d = 17\,\mathrm{rad\,s^{-1}}$) are shown in Fig. 7. Both $E(x)$ and $\mu(x)$ are affected by changes in the amplitude M and location a of the actuation and need not always have positive values. When the actuation is a single concentrated moment, the required modulus of elasticity reaches a maximum close to the caudal peduncle region ($x \sim 0.75l$). For a given magnitude M, moving the actuation location a toward the front of the body ensures that $E(x)$ remains positive until $x \sim 0.8l$. Increasing a creates a negative-valued region around $x \sim 0.35l$ (see Fig. 7a). For a given actuation location, increasing the moment amplitude increases peak values (see Fig. 7b). In all scenarios, $E(x)$ displays a negative region at the caudal end, $x > 0.85l$.

With the same actuation, the required viscosity is negative for most of the frontal part of the body and reaches a positive maximum in the caudal fin region at $x \sim 0.9l$. Moving the actuation location toward the front of the body increases the

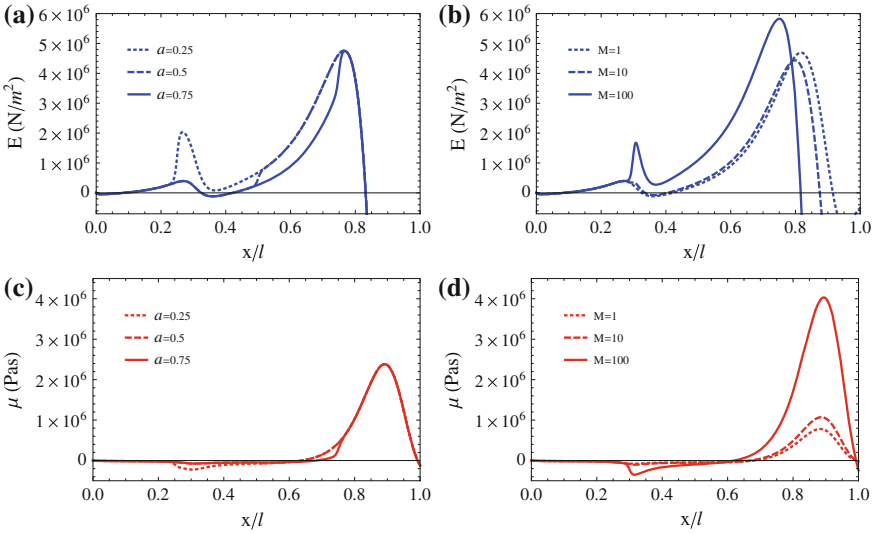

Fig. 7 Required modulus E and viscosity μ distributions along the length of a carangiform body of length $l = 1$ m undergoing forward swimming motions as defined by Eq. (1) and the parameters in Table 3 ($\omega = \omega_d = 17\,\text{rad}\,\text{s}^{-1}$). Distributions are continuous and differentiable. **a** Effects of actuator location $a[m]$ on $E(x)$. **b** Effects of actuation magnitude $M[N]$ on $E(x)$. **c** Effects of actuator location $a[m]$ on $\mu(x)$. **d** Effects of actuation magnitude $M[N]$ on $\mu(x)$

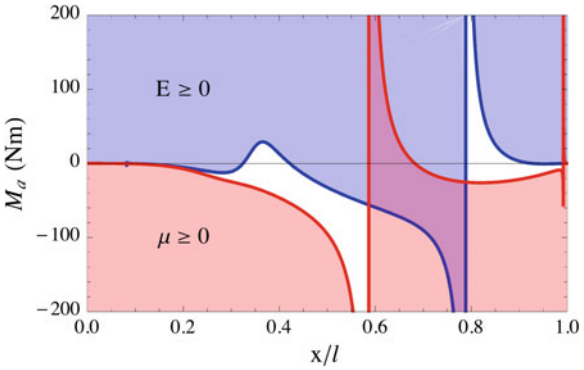

Fig. 8 Bounds for actuation distribution to achieve positive material distributions. *Blue* region satisfies the condition $E \geq 0$, and *red* region satisfies the condition $\mu \geq 0$. Overlapping regions satisfy both conditions and can be used to guide the selection of an actuation distribution $M_a(x)$

negative region (see Fig. 7c). Increasing actuation amplitude increases the values of positive ($x \sim 0.9l$) and negative ($x \sim 0.3l$) peaks (see Fig. 7d).

Materials displaying negative modulus of elasticity and negative viscosity are physically realizable, but are more challenging to manufacture. Instead, the analysis of Eq. (11) can provide guidelines for the actuation distributions that would yield

positive values for both $E(x)$ and $\mu(x)$. Figure 8 shows actuation bounds that would guarantee both $E(x)$ and $\mu(x)$ are positive. The bounds are found by solving the system of inequalities $E \geq 0,\ \mu \geq 0$. The region in blue represents the actuation distribution that would ensure $E \geq 0$ for $x \in [0, l]$ and the region in red represents the actuation distribution that would ensure $\mu \geq 0$ for $x \in [0, l]$. The overlapping regions satisfy both conditions and can guide the construction of an actuation distribution.

This example shows a simple implementation of the soft underactuated robot design methodology. Practical issues regarding proper manufacturing are addressed in Sect. 4.

2.5 Optimization

The problem of solving for material and actuation properties can also be set as a constrained optimization. Minimizing the number of actuators, actuation amplitude, or energy consumption, and maximizing efficiency, swimming speed, or thrust are all feasible. Initial work in this area of optimization can be found in [21]. In this study details of this approach are omitted, but the performance models presented in Sect. 5 are linked to body kinematics and can hence be used to solve for material and actuation properties. This particular approach will be presented in more detail in future studies.

3 Soft Body Fish Designs

Prototyping and actuating a soft viscoelastic fish-like body with the required material property distributions $E(x)$ and $\mu(x)$ described by Eq. (11) present several challenges. A mechanical implementation of concentrated moments and forces can be achieved with standard actuation. While the mechanisms used at this stage are not entirely soft, they allow the feasibility of the proposed approach to be tested. Fabrication of the required continuous material distributions is more challenging and a simple casting approach that can approximate the required distributions is discussed.

Figure 9 shows two examples of mechanisms used to approximate a concentrated moment inside flexible viscoelastic bodies. The torque of a servomotor is transferred to a plate through a four-bar-linkage type flexure (see Fig. 9a) or a cable connection (see Fig. 9b). The servo mounting base and the plate are embedded at different locations inside the flexible body and are made of materials at least one order of magnitude stiffer than the flexible body continuum. As a result the actuation creates bending in the viscoelastic body about an axis located in between the servo and the plate. In both cases, the flexure and cable regions need to move independently of the surrounding body which requires a low shear modulus material layer (lubrication) surrounding the moving components.

Figures 10 through 13 show designs of soft robot fish inspired by carangiform and thunniform swimmers. Internal components are fabricated using fusion

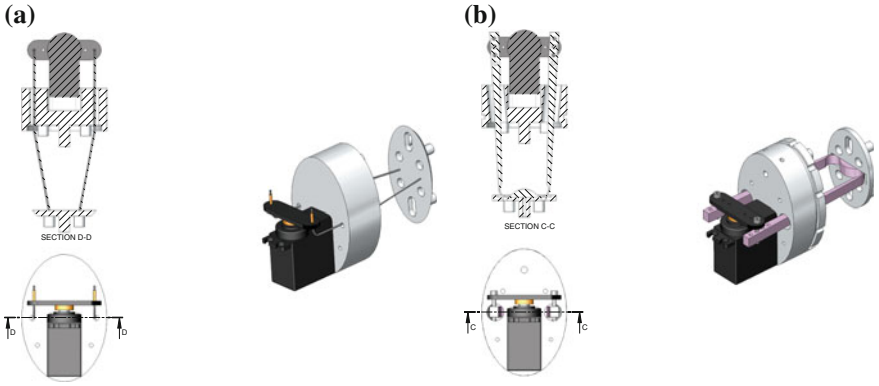

Fig. 9 Concentrated moment actuation. A servomotor is mounted to a stiff base embedded within a viscoelastic body (body not shown in drawings). The motor shaft is connected to a stiff plate, also embedded inside the flexible body at a distance away from the stiff base. Two designs allow force transmission from the servomotor to the stiff plate: **a** Cable/tendon drive. **b** Four-bar linkage flexure

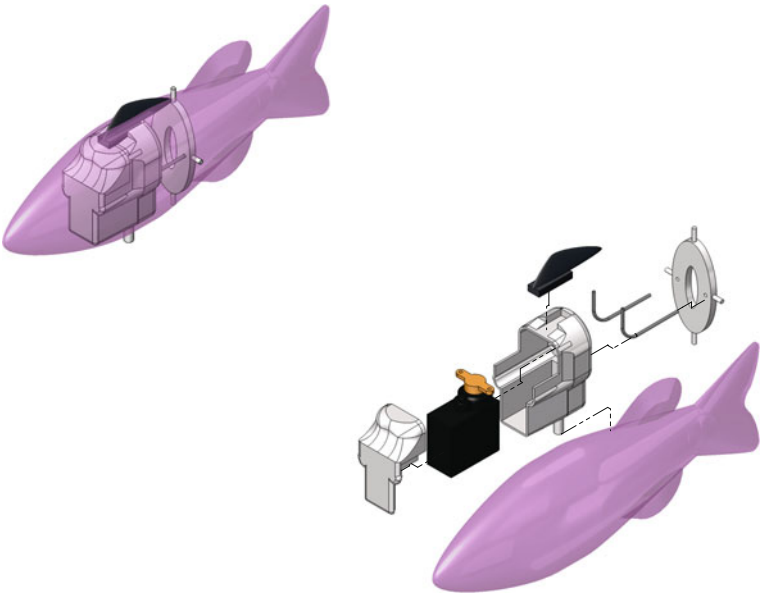

Fig. 10 Design for a soft robot fish inspired by a bass. Carangiform-like body with a caudal fin, two dorsal fins, and one anal fin. Body is powered by a single servo. The design consists of eight individual components including the viscoelastic body

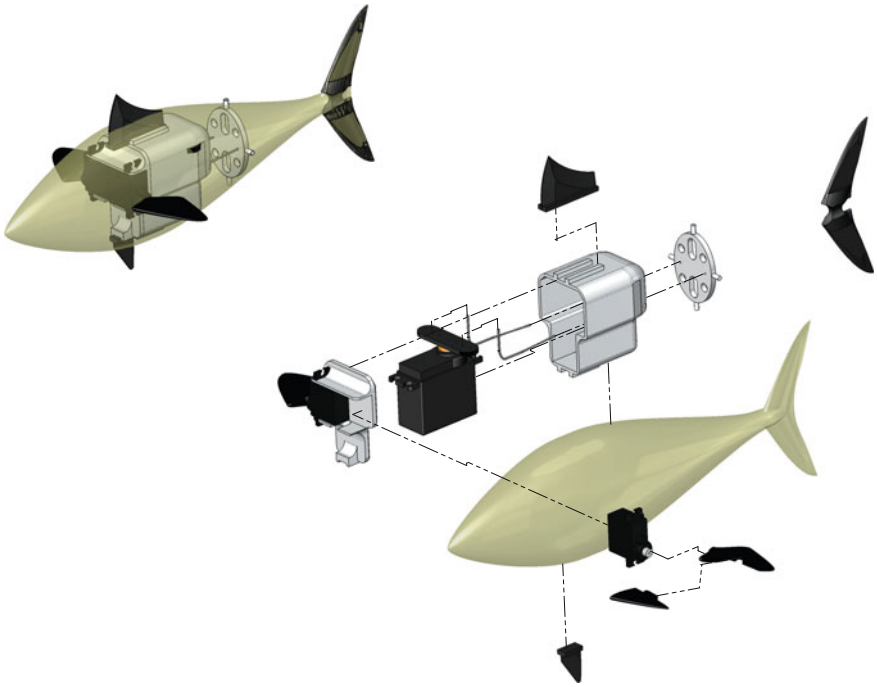

Fig. 11 Design for a soft robot fish inspired by a mackerel. Thunniform-like body with two individually controlled lateral fins, one dorsal fin, one ventral fin, and a high aspect ratio caudal fin. Body motions are powered by a single servo. The design consists of 16 individual components including the viscoelastic body

deposition manufacturing with ABS and polycarbonate plastics. Designs are simple, robust, and involve small part numbers compared to traditional bio-inspired robots. One actuator is sufficient to excite modes of vibration required for forward locomotion. Figure 10 shows the design of a carangiform type swimmer inspired by a bass. The design uses a cable-driven actuation unit and only 8 components are needed including the flexible body. Figure 11 shows the design of a thunniform type swimmer inspired by a mackerel. The design uses a cable-driven actuation unit and has two independently driven pectoral fins. The design consists of 16 components including the flexible body. Figure 12 shows the design of a thunniform type swimmer inspired by a shark. The design uses a flexure-driven actuation unit and has two independently driven pectoral fins. The prototype is fully autonomous and has power (lithium-ion cells) and a control unit (single board computer) embedded within the body. The design consists of 16 components including the flexible body. Figure 13 shows the design of a thunniform type swimmer inspired by a tuna. The design uses a cable-driven actuation unit and has two independently

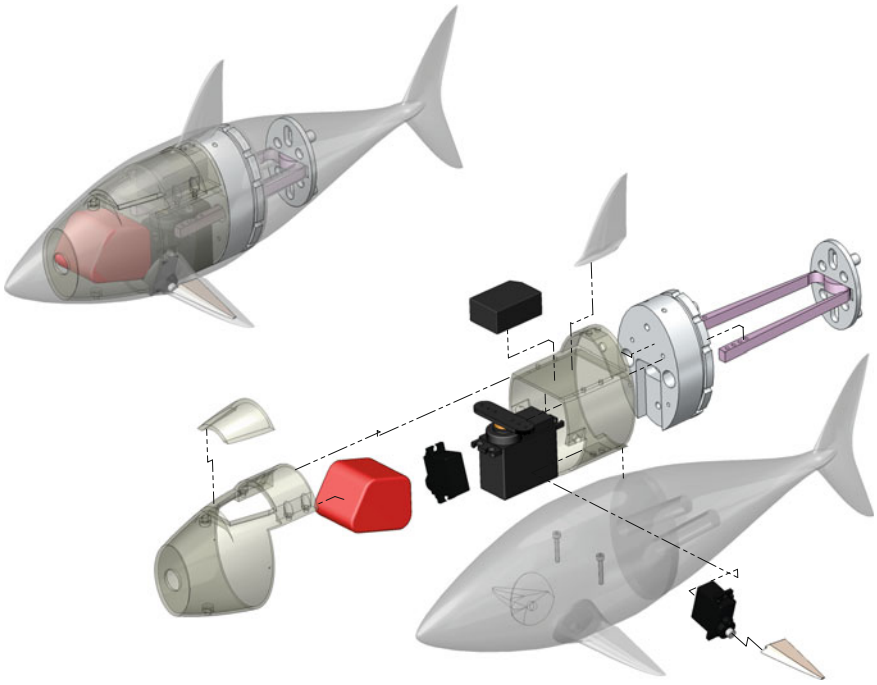

Fig. 12 Design for a soft robot fish inspired by a shark. Thunniform-like body with two individually controlled lateral fins, one dorsal fin, and a high aspect ratio caudal fin. Body is powered by a single servo. The design consists of 16 individual components including the viscoelastic body. Batteries and control unit are embedded inside the body

driven pectoral fins. The prototype is fully autonomous and has power (lithium-ion cells) and a control unit (single board computer) embedded within the body. The design consists of 21 components including the flexible body. The robotic mackerel, shark, and tuna designs have more streamlined peduncles and higher aspect ratio caudal fins with inserts to increase flexural rigidity. All prototypes are neutrally buoyant and do not use buoyancy control units. The mackerel, shark, and tuna designs control depth by changing lift forces as they swim forward using individually controlled pectoral fins. The fins also enable yaw and pitch turns as well as limited roll motions. Standard servomotors are used for simplicity but the approach can also be used with more sophisticated actuation such as electroactive polymers [3]. Wireless communications are used to update and control autonomous units.

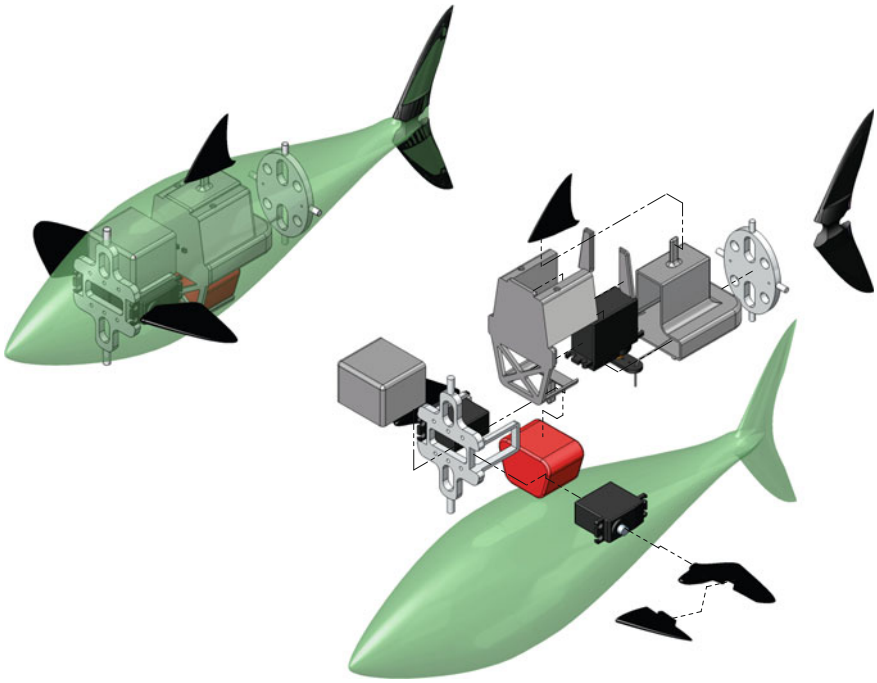

Fig. 13 Design for a larger scale soft robot fish inspired by a tuna. Thunniform-like body with two individually controlled lateral fins, one dorsal fin, and a high aspect ratio caudal fin. Body is powered by a single servo. The design consists of 21 individual components including the viscoelastic body. Batteries and control unit are embedded inside the body

4 Fabrication

Continuous material distributions as in Eq. (11) are needed to achieve a flexible body with the proper modes of vibration. At present, these types of distributions cannot be easily manufactured via standard or rapid prototyping techniques. The required material distributions are instead discretized and cast sequentially using silicone polymers. Given the symmetry of carangiform and thunniform geometries, a two part mold is often sufficient to cast the body. Pectoral fins can be added through a secondary casting process. The concept and the steps involved in the casting process are shown in Fig. 14. A two part mold of the fish-like volume is machined from a wax block. The molds can also be printed using fused deposition manufacturing (FDM) or other three-dimensional printing technologies. The advantage of wax and the plastics used in FDM is that they naturally do not form a chemical bond to silicone polymers and the application of a thin mold release layer is enough to facilitate demolding.

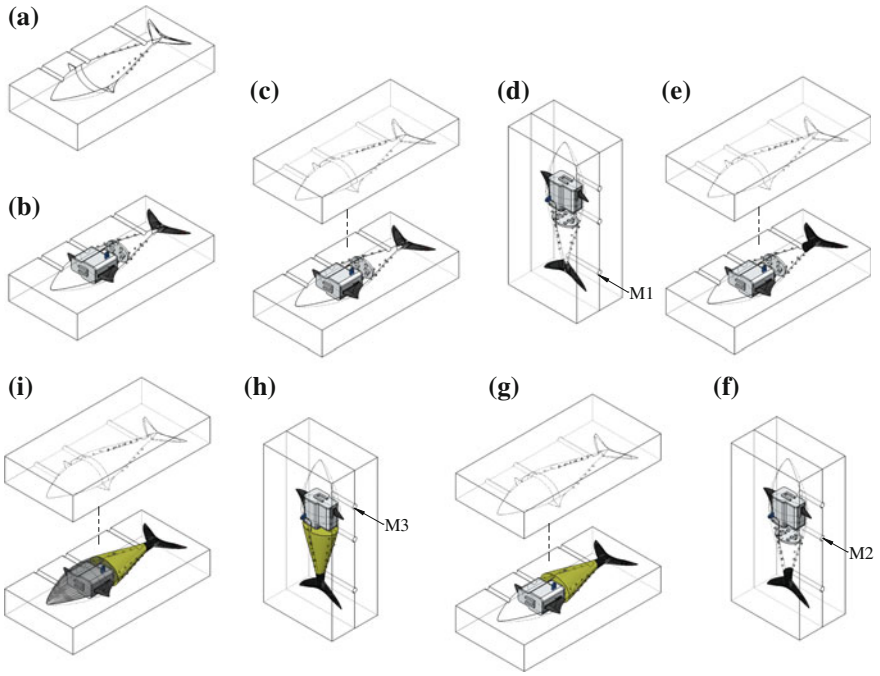

Fig. 14 A two part mold is used for fish-like bodies. Mold components are 3D printed or machined from wax blocks and material distributions are approximated using casting techniques. The original modulus and viscosity distributions are discretized in *n* sections and each section is casted consecutively using different viscoelastic polymers with matching material properties. The steps shown are for a thunniform prototype where the flexible body is cast with three different material regions. Manufacturing steps: **a** A mold half with three molding ports is prepared for casting; **b** internal components are positioned inside the mold half; **c** opposite mold half is aligned and the mold is closed; **d** first material (M1) is poured in and mold is oriented to constrain material location during curing; **e** after curing mold is opened to remove any material excess; **f** mold is closed, a second material (M2) is poured in and the mold is reoriented for curing; **g** after curing mold is opened to remove material excess; **h** mold is closed, third and last material (M3) is poured in, and the mold is reoriented for curing; **i** after final curing the mold is opened and the prototype is ready

Figure 14a shows a mold half with three molding ports. Previously printed internal mechanisms and housing components are positioned inside the mold half as shown in Fig. 14b. The opposite mold half is aligned and the mold is closed (Fig. 14c). The mold is reoriented to allow proper leveling during the casting process (Fig. 14d). The discretized material distribution is cast by sections starting from one end of the body. An appropriate number of ports should be added in a mold accordingly. Section lengths are controlled through the volume of silicone polymer poured inside the mold and any excess can be removed after demolding. Figure 14e shows the mold being opened for material excess removal after casting the tail section. After excess removal the mold is closed and reoriented to enable

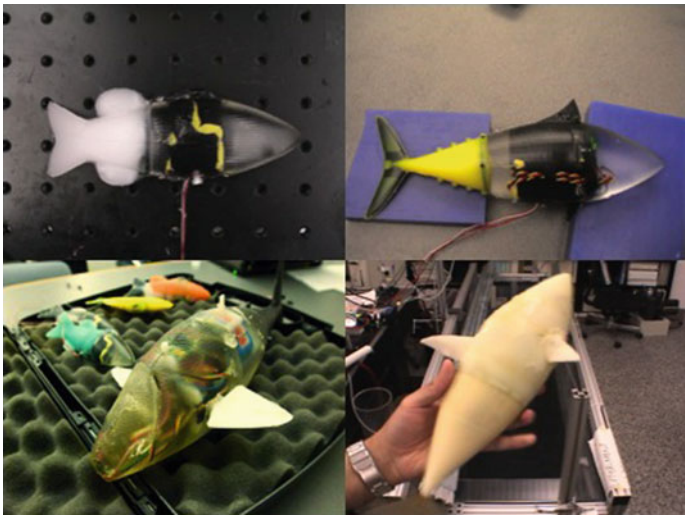

Fig. 15 Finished prototypes. Clockwise from *top left* small carangiform body (*bass*) resulting from design in Fig. 10, medium-sized thunniform body (*mackerel*) resulting from design in Fig. 11, medium-sized thunniform body (*shark*) resulting from design in Fig. 12, larger sized thunniform body (*tuna*) resulting from design in Fig. 13. Different viscoelastic materials appear with different *colors*

casting of the following section as shown in Fig. 14f. Newly cast silicone sections form a chemical bond with previously cast sections provided common surfaces are not contaminated during the process. The casting process continues in the same manner, section by section until the body is complete (Fig. 14g–i). The example body shown in Fig. 14 only has three discrete sections.

Platinum cure silicone rubbers are used for casting body sections due to the compatibility of their material properties with required modulus and viscosity ranges. Silicone rubbers cure at room temperature but the process can also be accelerated using an oven. Different silicone compounds were characterized using a dynamic mechanical analyzer [21]. The viscoelastic behavior of silicone polymers is highly nonlinear but for moderate strains, the constitutive relations governing stress–strain relations can be reasonably approximated by Eq. (4).

Figure 15 shows four completed prototypes of the designs in Figs. 10 through 13. Different materials can be distinguished by their color and surface appearance. The body surface in all prototypes is continuous and discontinuity-free as a result of the casting process. All delicate components are encapsulated inside the bodies and protected from external environment conditions.

Unfortunately, discretization of the continuous material distributions can lead to errors in body motions and a decrease in locomotion performance. In addition, within a discrete section, a single material often cannot satisfy both required modulus of elasticity and viscosity values. A simple solution is to attempt to match

the required viscosity first, and correct modulus discrepancies with purely elastic embedded structures. Future work on material synthesis is crucial as is the capability to tailor material constitutive relations.

5 Locomotion Performance

Locomotion performance is characterized using three parameters: average forward swimming speed U, propulsive thrust T, and locomotion efficiency η. Based on Lighthill's elongated body theory [15], simple locomotion performance models can be derived.

The average forward propulsive thrust, T, can be approximated by,

$$T \sim m_l H_l^2 \left(\omega^2 - U^2 \left(\kappa^2 + \frac{1}{l^2} \right) \right) \tag{12}$$

where H_l and m_l are the peak-to-peak oscillation amplitude and the added mass at the caudal fin tip ($x = l$), respectively. The average swimming speed, U, can be approximated by,

$$U \sim \omega H_l \sqrt{\frac{m_l}{\rho_f C_d l^2 + m_l H_l^2 \left(\kappa^2 + \frac{1}{l^2} \right)}} \tag{13}$$

where C_d is the estimated body drag coefficient. The total propulsive efficiency η is given by,

$$\eta = \frac{UT}{vi} \tag{14}$$

where v and i are the voltage supplied and the current consumed by the prototype's actuators. The body kinematics can also be approximated by simplifying Eq. (2) using an order of magnitude analysis. The caudal fin peak-to-peak oscillation amplitude H_l can be approximated as,

$$H_l \sim \frac{M}{(l-a)^2 \sqrt{\left(\frac{EI}{(l-a)^4} - (\rho A + m_l)\omega^2 \right) + \left(\frac{\mu I \omega}{(l-a)^4} \right)}} \tag{15}$$

and the wave number κ is given by,

$$\kappa = \frac{1}{l} \tan^{-1} \left(\frac{\frac{\mu I \omega}{(l-a)^4}}{\frac{EI}{(l-a)^4} - (\rho A + m_l)\omega^2} \right) \tag{16}$$

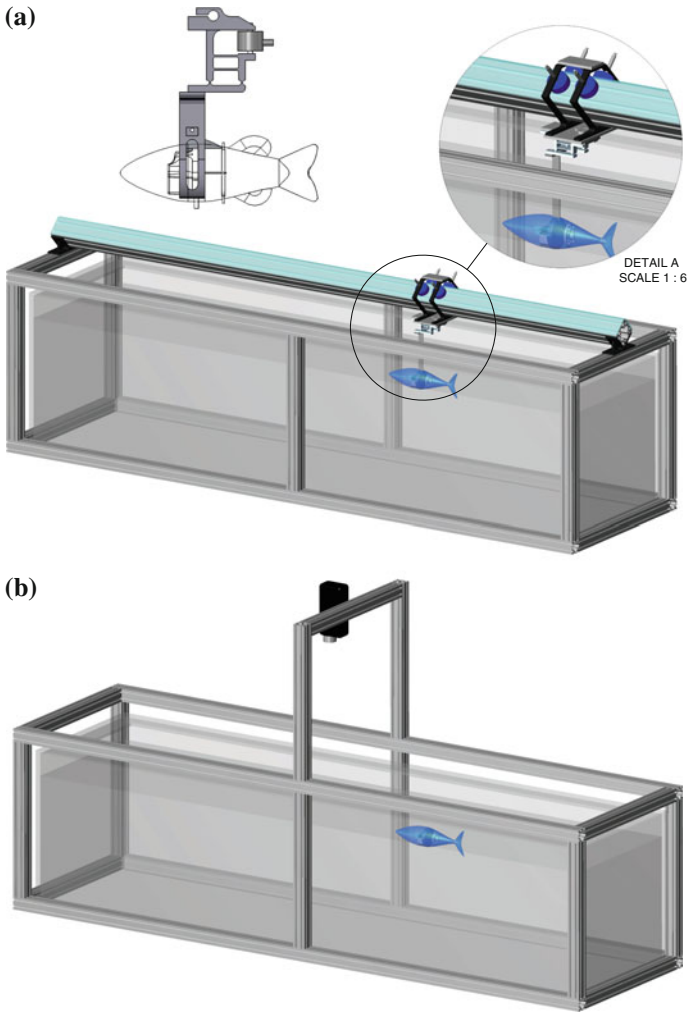

Fig. 16 Experiment setup: 2m × 0.5m × 0.5m acrylic tank surrounded by aluminum frame. **a** A beam support for an air-bearing carriage is mounted along the length of the tank. The carriage is fitted with a tension–compression load cell for propulsive force measurements. **b** An overhead camera is used for the free swimming and body kinematics experiments

Three different experiments were used to test the models in Eqs. (12) through (16): propulsive force measurements, free-swimming speed measurements, and free-swimming kinematic analysis. Details of the experimental setup are shown in Fig. 16. The main testing apparatus consists of a 2 m long, 0.5 m wide, and 0.5 m deep water tank. The tank was built using transparent acrylic sheets to provide visibility of its contents from a wide variety of angles. An aluminum frame surrounds the tank and it is used to mount cameras, lighting, and other testing

equipment. An aluminum beam can be mounted on top and along the length of the tank to support a carriage. Prototypes can be mounted to the carriage bottom which is outfitted with load cells to enable propulsive force measurements. The carriage frame is fabricated entirely of low-density plastics to minimize inertia and it is supported by four vacuum preloaded air bearings to minimize friction. To accommodate the surface finish required to use air bearings in a long test section two long float glass strips are glued to the upper beam surfaces. The glass surface finish satisfies the bearings surface roughness requirements. More details of the carriage design and bearing arrangement can be found in [21].

Measuring propulsive thrust in free swimming is challenging. Propulsive forces can be estimated using particle image velocimetry (PIV) as in Epps et al. [11], or by analyzing the vortex wake geometry and kinematics as proposed by Valdivia y Alvarado [27]. A simple estimate can be obtained by measuring the static forces generated as a prototype is actuated to move. Prototypes are mounted to the carriage and held static inside the water tank. A tension–compression load cell arrangement in the carriage bottom supports a prototype and enables measurements of the forces generated during forward propulsion (see Fig. 16a). As the prototypes are actuated to move, the inline forces generated are recorded by the load cell arrangement. All experimental results in this section are obtained using the small carangiform prototype design shown in Fig. 10. The prototype used had a length $l = 0.15$ m and an average density $\rho = 900\,\mathrm{kg/m^3}$.

Figure 17 shows measured static thrusts versus caudal fin flapping frequencies along with the model prediction based on Eq. (12) for a small bass prototype. Static thrust measurements are an upper bound estimate of free-swimming thrust values at a given frequency. As expected, the model underestimates measured static thrust values but is capable of predicting a peak thrust attained at the design frequency $\omega_d = 17(\mathrm{rad\ s^{-1}})$.

Free-swimming velocities and swimming kinematics are recorded inside the same tank using an overhead camera (see Fig. 16b). Prototypes have three markers

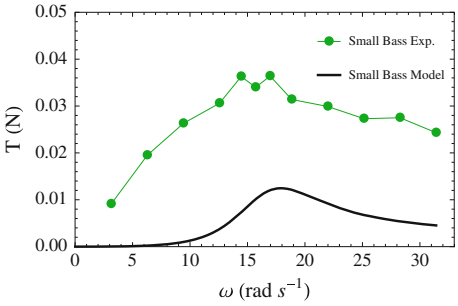

Fig. 17 Measured static thrust T versus model prediction on a small carangiform prototype. Static thrust measurements are expected to be larger than free-swimming values at a given frequency. The model underestimates, as expected, static thrust values but correctly predicts that a peak thrust is attained at the design frequency $\omega_d = 17(\mathrm{rad\ s^{-1}})$

attached along their dorsal (top) edge: one marker at the frontal tip, a second marker close to the center of mass, and a third marker at the tip of the caudal fin. A MATLAB routine is used to post-process footage of the free-swimming runs and track marker locations. The largest prototype tested inside the tank had a body length l = 0.3 m so wall effects were negligible. Figure 18a shows a sample image of the overhead view of a bass prototype during free swimming, a series of superimposed processed images showing the trajectories of the three markers are shown in Fig. 18b, and the corresponding marker trajectories versus time are shown in Fig. 18c. Figure 19a shows measured caudal fin peak-to-peak flapping amplitude H_l for the same bass prototype, obtained from the trajectory of the marker placed at

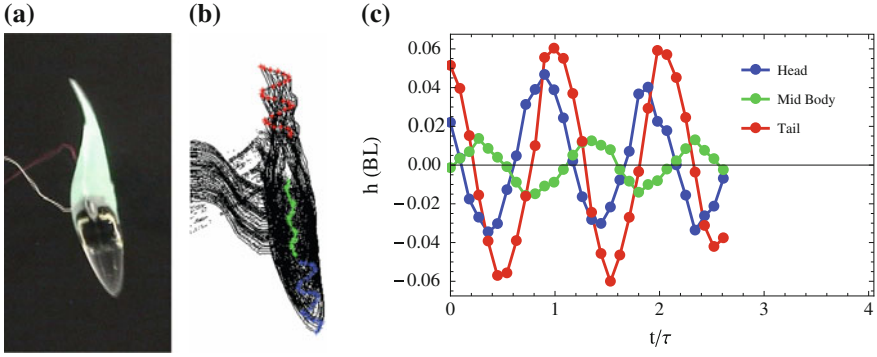

Fig. 18 **a** *Top view* of a small carangiform prototype during free swimming. **b** Superimposed contours of the prototype body during free swimming. Markers are located at the front tip (*blue*), center of mass (*green*), and caudal fin tip (*red*). **c** Trajectories of body markers, with respect to body average trajectory, plotted versus time. Both wavelength λ and wave number κ can be calculated from the phase differential between font tip and caudal fin marker trajectories. H_l is obtained from the amplitude of the caudal fin marker trajectory

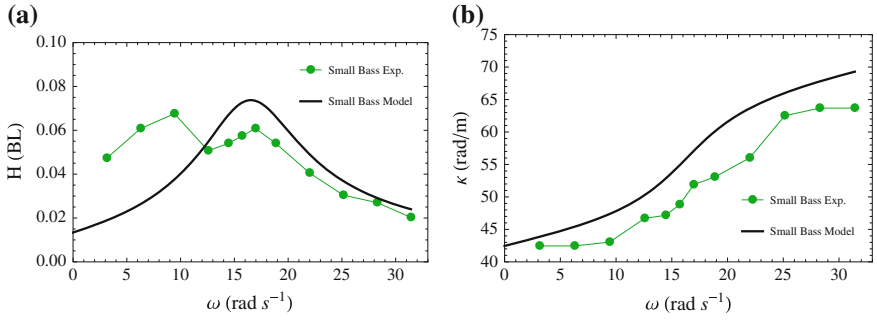

Fig. 19 **a** Caudal fin peak-to-peak flapping amplitude H_l measurements and model prediction versus fin flapping frequency. **b** Measured wave number κ and model prediction versus flapping frequency

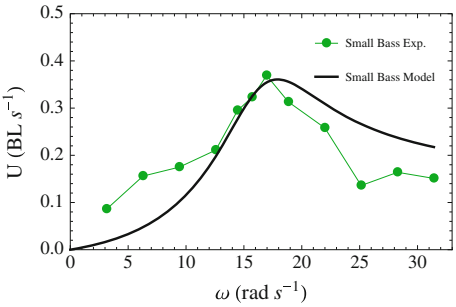

Fig. 20 Measured average swimming velocity U versus model prediction on a small carangiform prototype. The model uses a drag coefficient C_d estimated by towing the unactuated body at different speeds. The model correctly predicts a peak velocity occurs at the design frequency $\omega_d = 17(\text{rad s}^{-1})$

the caudal fin tip, versus the prediction from Eq. (15). The measured wave number κ, based on the phase between the trajectories of the front and caudal fin markers, and the prediction from Eq. (16) is shown in Fig. 19b. Average swimming speed U versus caudal fin flapping frequencies is shown in Fig. 20 along with model predictions based on Eq. (13).

To measure propulsive efficiency, the voltage v supplied and the current i consumed by all actuators were recorded. The prototypes used in the experiments are connected to an external power source. The connection cables are flexible and thin so as to minimize any interference with the prototype's natural swimming motions. The total propulsive efficiency η can be decomposed as,

$$\eta = \eta_a \times \eta_b \times \eta_h \tag{17}$$

where η_a is the actuation efficiency, η_b is the body transmission efficiency, and η_h is the hydrodynamic efficiency of swimming motions. η_a depends on the actuation technology and control approach used. η_h depends on body motions. η_b is the efficiency at which an underactuated soft body transfers actuation power to the body–liquid medium interface and it is a key performance parameter to evaluate the approach. The individual efficiencies are given by [21],

$$\eta_a = \frac{M \frac{\partial h}{\partial x \partial t}|_a}{vi} \tag{18}$$

$$\eta_b = \frac{Um\omega^2 H_l^2 \left(1 - \frac{U}{V}\right)}{M \sin(\kappa a) \frac{\partial h}{\partial x}|_a} \tag{19}$$

$$\eta_h = \frac{1}{2}\left(1 + \frac{U}{V}\right) - \frac{1}{2}\left(\frac{U}{\omega}\right)^2 \left(1 - \frac{U}{V}\right)^{-1} \left(\frac{\frac{\partial h}{\partial x}|_l}{H_l}\right)^2 \tag{20}$$

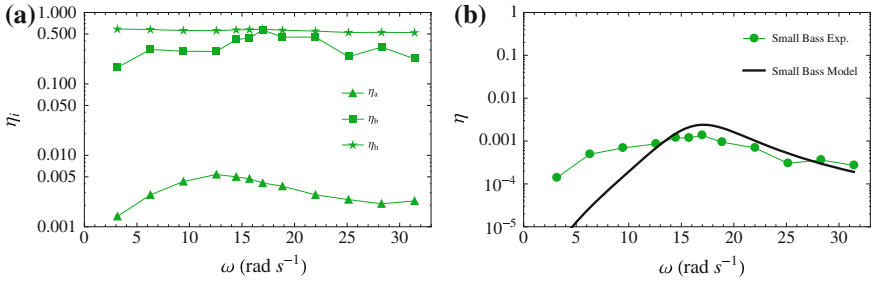

Fig. 21 **a** Predicted body efficiency η_b, predicted hydrodynamic efficiency η_h, and measured actuator efficiency η_a. **b** Measured total efficiency η against model prediction

Figure 21 shows measured and estimated system efficiencies. Predicted values for η_b and η_h, and measured values η_a versus fin flapping frequency are shown in Fig. 21a. The body and hydrodynamic efficiencies cannot be easily measured but model predictions, using measured values for H_l, U, V, and κ, provide some intuition on the mechanism performance. Both predicted body and hydrodynamic efficiencies display a maximum value at the design frequency $\omega_d = 17\,\mathrm{rad\,s^{-1}}$. Hydrodynamic efficiencies agree with values estimated by earlier studies. Predicted body efficiencies are encouraging, at the design frequency the soft body transmission has an efficiency in the order of 50 %. A traditional discrete-stiff mechanism would require a complex transmission and likely result in a much lower body efficiency. Actuation efficiency is low, as servos are driven to oscillate the constant change in acceleration draws current whose corresponding power is lost as heat in the actuator coils. Figure 21b shows model predictions and measurements for the total system efficiency η. Measured total efficiency agrees with model predictions and its low values are explained by the low actuation efficiency.

Figure 22 shows snapshots of the wake generated by the prototype captured using fluorescent dye flow visualizations. Details of the setup and image processing can be found in [11]. Flow visualization and PIV studies confirmed the existence of

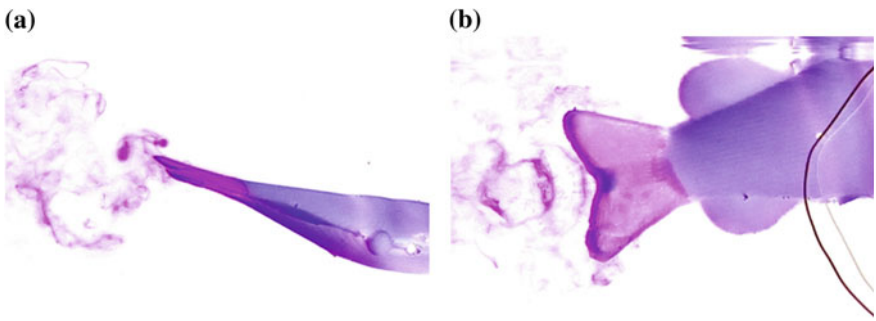

Fig. 22 Dye flow visualization of carangiform prototype: **a** *Top view*, a single vortex is just shed into the wake. **b** *Side view*, a chain of vortices akin to an inverted von karman street can be seen streaming from the caudal fin

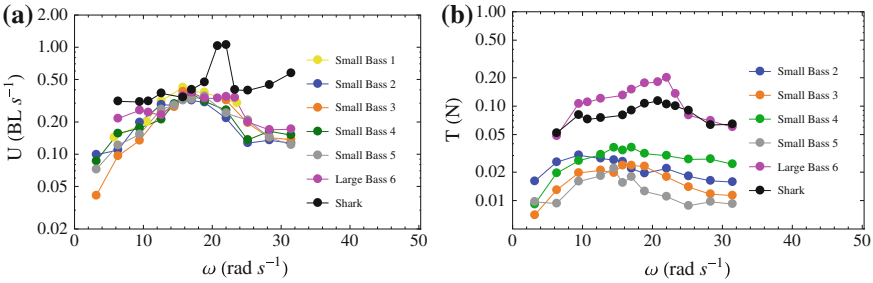

Fig. 23 **a** Measured average swimming velocities U for different prototypes. **b** Measured static thrusts T for different prototypes

a thrust generating wake streaming from the prototype's caudal fin [11]. Figure 22a shows a top view of the prototype swimming and a vortex just being released from the edge of the caudal fin. Figure 22b shows a side view of the prototype swimming. Two vortices can be seen forming a chain emanating from the caudal fin edge. Due to errors in body kinematics, the wake generated was not exactly an inverted von karman wake or 2S wake, but rather a series of vortex pairs forming a wide wake similar to a 2P wake.

Many more prototypes, both carangiform and thunniform, were tested to validate the design methodology. The results, regardless of scale, confirmed a peak in performance at the design frequencies. Figure 23 shows average swimming speeds and static thrusts for several other prototypes. The maximum swimming speed achieved at a design frequency is $U_{\max} \sim 1\,BL\,\mathrm{s}^{-1}$. Among the prototypes built for the original study on underactuated soft robot fish, the first failure due to operational wear occurred after 3 years of regular monthly testing. The failure mode thus far has only been related to the servomotors used for actuation.

6 Discussion

The design methodology introduced in Sect. 2 was tested using several carangiform and thunniform prototypes. Sect. 3 presented examples of robots and actuation unit designs and Sect. 4 described the manufacturing techniques used to fabricate underactuated soft robots. The performance results for a small carangiform design summarized in Sect. 5 confirm the approach basic claim: the natural dynamics of a flexible viscoelastic body can be excited by a simple mechanism to replicate complex bio-inspired locomotion kinematics and performance. In addition, the efficiencies displayed by the soft body transmissions are high and failure modes are related to actuation. Body transmissions maintain their mechanical robustness for extended time periods.

The implementation of the proposed approach on fish-like forward locomotion kinematics (Eq. 1) highlights several advantages. A continuous flexible body with a

characteristic heterogeneous material distribution is simple, robust, and protects all encapsulated delicate components. Mechanism robustness is tied to material properties and polymer materials present several desirable attributes for operation within liquid environments. The platinum cure silicones used in this study display low permeability, ultraviolet and high temperature resistance, as well as corrosion and biofouling resistance. Furthermore, a continuous body has by definition an infinite number of DOFs which enable more natural motions.

The experiment results in Sect. 5 confirm that a flexible body can be manufactured to display natural dynamics that mimic body motions during fish locomotion. The caudal fin oscillation amplitude H_l, wave number κ, average swimming speed U, and propulsive forces T agree qualitatively with model predictions. A coarse discretization of the required material distributions leads to errors in body motions which in turn diminish the prototype performance with respect to real fish.

While these results are encouraging, a soft continuous structure is inherently more challenging to control because of the large number of DOFs involved. Furthermore, the choice of underactuation as a means to simplify the mechanism limits the controllable state space. The proposed approach exploits the natural body dynamics to achieve low-level control tasks. Actuation does not force the mechanism to track a particular trajectory, the natural dynamics of the mechanism should match the desired trajectories. As a result, if different behaviors are needed then new structural dynamics are also required. A solution requires dynamic control of local material properties. Different approaches can be taken toward achieving material property control (e.g., using temperature phase changes, granular packing, etc.) but low power [23] or passive approaches should be favored for mobile robot applications.

Power sources and actuation still require stiff and rigid components. At present rechargeable batteries are still the most practical option to power robots. However, standard battery energy densities are not sufficient to satisfy the requirements for long range and long-term deployments. Work on different forms of energy transduction and opportunistic use of environmental resources is essential to advance this area.

Actuation is an area that is closer to having full or partial soft solutions. Work on various artificial muscle actuators, a term broadly used for actuation mechanisms that are similar in function to animal muscle, has matured and practical implementations are closer to being a reality [3].

7 Conclusions

The methodology presented in Sect. 2 was first applied to mobile robots mimicking carangiform and thunniform fish where target body kinematics (traveling waves) are restricted to a single plane [21, 28–30]. However, the concept can easily be applied to more complex kinematics. Valdivia y Alvarado et al., applied the

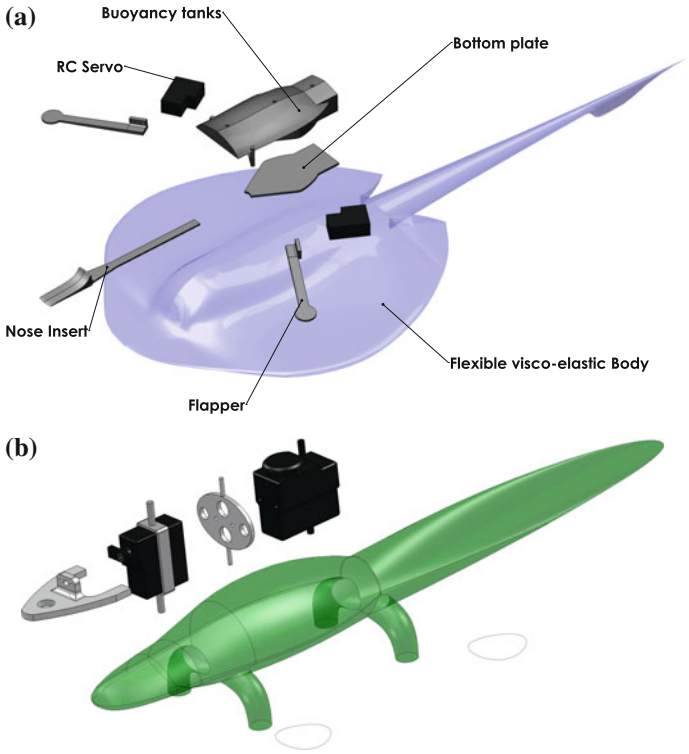

Fig. 24 **a** Batoid design: traveling waves with azimuthal and radial components for thrust vectoring. **b** Salamander design: torsional mode coupled with body mode to achieve walking and swimming

methodology to design batoid-like robots (see Fig. 24a) [8, 9, 22, 24, 26] and salamander-like robots (see Fig. 24b) [25] where required body motions involve vibrations with components along different planes. In the case of batoids, locomotion requires three-dimensional traveling waves along large pectoral fins. In the case of salamanders, locomotion involves a combination of traveling waves (swimming) and standing waves coupled with body torsion (walking). The mechanisms required to excite body modes are as simple as the resulting robots.

Several groups have also adopted similar approaches to improve mechanical robustness and test locomotion performance and control ideas. Kruusmaa et al. (FILOSE project) designed and built robotic fish inspired by the present approach [1, 10]; Strefling et al. [19] developed a jet-driven fluttering fluid-conveying flexible tail propulsion mechanism which exploited tail flexibility; Marchese et al. [16] developed soft fish-like robots to test pneumatic and hydraulic actuation and control three-dimensional motion; Kopman et al. [13] designed a robotic fish propelled by a compliant tail. These works along with many others collectively demonstrate the advantages found by exploiting body flexibility.

Due to the nature of the approach its application is better suited for periodic motions where the environment favors inertia forces. Bio-inspired locomotion in fluids when high Reynolds numbers define the dynamics is an ideal example, but several applications in manipulation and grasping fit those requirements just as well.

Modeling plays a key role in finding proper material distributions to accomplish desired body motions. However, a balance must be struck between the model complexity and practical manufacturing limitations. At present, continuous material distributions cannot be easily manufactured. A discrete approximation is needed so that casting or other deposition-based manufacture can be used. Complex models provide more accurate distributions but simpler models can often be solved analytically and provide more physical intuition.

The required material distributions are unique to a particular target motion and actuation setup. Different motions are still possible with a given material distribution but only the original target kinematics are matched accurately. In order to better adapt to different or changing motion requirements a dynamic control of material properties at the local level is needed. Using controlled temperature phase changes as in Cheng et al. [6, 7], jamming as in Kime et al. [12], or small pre-strain changes with embedded mechanisms as in Valdivia y Alvarado and Bhat [23] can enable such changes and should be further explored.

The simplicity and robustness of underactuated soft robots is an ideal attribute and enabling feature for mobile robots targeting long-term deployments in harsh environments. The examples presented herein use inorganic silicone polymers but organic and biodegradable compounds can also be used to diminish environmental concerns when a fleet of soft robots explores an ecosystem. Challenges remaining include power, actuation, and electronics which still use standard hardware components.

Acknowledgments The authors would like to acknowledge the help and contributions of past and present collaborators in this project: A. Mazumdar, S. Chin, B. Epps, B. Blackburn, F. Yuen, and A. Cloitre.

References

1. Akanyeti et al (21 authors) (2014) FILOSE: a svenning* robot. IEEE Robot Autom Mag
2. Antman SS (2005) Nonlinear problems of elasticity, 2nd edn. Springer, New York
3. Bar-Cohen Y (2001) Electroactive polymer (EAP) actuators as artificial muscles: reality, potential, and challenges. SPIE Press, Bellingham
4. Barrett DS, Triantafyllou MS, Yue DKP, Grosenbaugh MA, Wolfgang MJ (1999) Drag reduction in fish-like locomotion. J Fluid Mech 392:183–212
5. Breder CM (1926) The locomotion of fishes. Zoologica (NY) 4(5):159–297 (Society for Industrial and Applied Mathematics, Philadelphia)
6. Cheng N, Ishigami G, Hawthorne S, Chen H, Hansen M, Telleria M, Playter R, Iagnemma K (2010) Design and analysis of a soft mobile robot composed of multiple thermally activated joints driven by a single actuator. In: Proceedings of the IEEE international conference on robotics and automation

7. Cheng N, Gopinath A, Wang L, Iagnemma K, Hosoi AE (2014) Thermally tunable, self-healing composites for soft robotic applications. Macromol Mater Eng. doi:10.1002/mame.201400017
8. Cloitre A, Subramaniam V, Patrikalakis N, Valdivia y Alvarado P (2012) Design and control of a field deployable Batoid Rotor. In: Proceedings of the IEEE international conference on biomedical robotics and biomechatronics (BioRob), Rome, Italy, pp 707–712
9. Cloitre A, Arensen B, Patrikalakis N, Youcef-Toumi K, Valdivia y Alvarado P (2014) Propulsive performance of an underwater soft biomimetic batoid robot. In: Proceedings the 24th international ocean and polar engineering conferences (ISOPE), Busan, Korea
10. El Daou H, Salumae T, Chambers LD, Megill WM, Kruusmaa M (2014) Modelling of a biologically inspired robotic fish driven by compliant parts. Bioinspr Biomim 9(1):016010
11. Epps B, Valdivia y Alvarado P, Youcef-Toumi K, Techet A (2009) Swimming performance of a biomimetic compliant fish-like robot. Exp Fluids 47(6):927–939
12. Kim Y, Cheng S, Kim S, Iagnemma K (2013) A novel layer jamming mechanism with tunable stiffness capability for minimally invasive surgery. IEEE Trans Robot 29(1):1031–1042
13. Kopman V, Laut J, Acquaviva F, Rizzo A, Porfiri M (2014) Dynamic modeling of a Robotic Fish propelled by a compliant tail. IEEE J Ocean Eng 99:1–13
14. Kubow TM, Full RJ (1999) The role of the mechanical system in control: a hypothesis of self-stabilization in hexapedal runners. Phil Trans R Soc Lond B 354:849–862
15. Lighthill MJ (1975) Mathematical biofluiddynamics. Society for Industrial and Applied Mathematics, Philadelphia
16. Marchese AD, Onal CD, Rus D (2014) Autonomous soft robotic fish capable of escape maneuvers using fluidic elastomer actuators. Soft Robot 1(1):75–87
17. McGeer T (1990) Passive dynamic walking. Int J Robot Res 9(2):62–82
18. Merz R, Prinz FB, Ramaswami K, Terk M, Weiss L (1994) Shape deposition manufacturing. In: Proceedings of the solid freeform fabrication symposium, University of Texas, Austin. Accessed 8–10 Aug 1994
19. Strefling PC, Helium AM, Mukherjee R (2012) Modeling, simulation, and performance of a synergistically propelled ichthyoid. IEEE/ASME Trans Mech 17(1):36–45
20. Timoshenko S, Young DH, Weaver W Jr (1974) Vibration problems in engineering. Wiley, New York
21. Valdivia y Alvarado P (2007) Design of biomimetic compliant devices for locomotion in liquid environments, doctoral dissertation. MIT, Cambridge
22. Valdivia y Alvarado P (2011) hydrodynamic performance of a soft body under-actuated batoid robot In: Proceedings IEEE international conference on robotics and biomimetics (ROBIO), Phuket Island, Thailand, pp 1712–1717
23. Valdivia y Alvarado P, Bhat S (2014) Whisker-like sensors with tunable follicle sinus complex for underwater applications In: Proceedings SPIE bioinspiration, biomimetics, and bioreplication IV conference, San Diego, CA, 9–12 March 2014
24. Valdivia y Alvarado P (In preparation) Design of soft batoid-like underwater robots
25. Valdivia y Alvarado P (In preparation) Design of soft amphibian robots
26. Valdivia y Alvarado P, Chin S, Larson W, Mazumdar A, Youcef-Toumi K (2010) A soft body under-actuated approach to multi degree of freedom biomimetic robots: a stingray example In: Proceedings IEEE RAS/EMBS international conference on biomedical robotics and biomechatronics (BIOROB), Tokyo, Japan, pp 473–478
27. Valdivia y Alvarado P, Sekar KS (Under Review) Modeling wake topology and thrust production in batoid-inspired oscillating fins
28. Valdivia y Alvarado P, Youcef-Toumi K (2003) Modeling and design methodology for an efficient underwater propulsion system. In: Proceedings IASTED international conference on robotics and applications, Salzburg, Austria, pp 161–166

29. Valdivia y Alvarado P, Youcef-Toumi K (2005) Performance of machines with flexible bodies designed for biomimetic locomotion in liquid environments. In: Proceedings IEEE international conference on robotics and automation (ICRA), Barcelona, Spain, pp 3324–3329
30. Valdivia y Alvarado P, Youcef-Toumi K (2006) Design of machines with compliant bodies for biomimetic locomotion in liquid environments. ASME J Dyn Sys Meas Cont 128:3–13